Review of Scientific Instruments

Gas puff imaging system for edge plasma fluctuation measurements in large helical device

Cite as: Rev. Sci. Instrum. **93**, 093513 (2022); https://doi.org/10.1063/5.0100301
Submitted: 23 May 2022 • Accepted: 28 July 2022 • Published Online: 21 September 2022

M. Kobayashi, S. Ohdachi, Y. Xu, et al.

Review of Scientific Instruments ARTICLE scitation.org/journal/rsi

Gas puff imaging system for edge plasma fluctuation measurements in large helical device

Cite as: Rev. Sci. Instrum. 93, 093513 (2022); doi: 10.1063/5.0100301
Submitted: 23 May 2022 • Accepted: 28 July 2022 •
Published Online: 21 September 2022

M. Kobayashi,[1,2,a)] S. Ohdachi,[1] Y. Xu,[3] W. Li,[3] A. Shimizu,[1,2] and J. Cheng[3]

AFFILIATIONS

[1] National Institute for Fusion Science, National Institutes of Natural Sciences, Toki, Gifu 509-5292, Japan
[2] National Institute for Fusion Science, SOKENDAI, The Graduate University for Advanced Studies, Toki, Gifu 509-5292, Japan
[3] Institute of Fusion Science, School of Physical Science and Technology, Southwest Jiaotong University, Chengdu, Sichuan 610031, China

Note: This paper is part of the Special Topic on Proceedings of the 24th Topical Conference on High-Temperature Plasma Diagnostics.
[a)] **Author to whom correspondence should be addressed:** kobayashi.masahiro@nifs.ac.jp

ABSTRACT

A gas puff imaging system has been developed to measure edge fluctuations in large helical device. The optical system splits the image of the plasma into four wavelengths, H_α/D_α (656 nm), HeI (1s2p–1s3d; 587.6; 1s2p–1s3d, 667.8; and 1s2p–1s3s, 706.5 nm), enabling simultaneous measurement of the spatial distribution of line ratios of He I. The image of the plasma is amplified with an image intensifier and recorded with a fast-framing camera. The measurement area has a diameter of 20 cm just outside of the last closed flux surface. The spatial resolution of the optical system is about 3 mm, and the frame rate is 100 kHz for acquisition of the four wavelength images. Signal-to-noise ratio is evaluated for the system, and further improvement is discussed. Clear images are obtained for all wavelengths and a slightly different pattern is recognized, depending on the wavelength. A singular value decomposition analysis can decompose the image clearly to one perpendicular and parallel to the magnetic field lines.

I. INTRODUCTION

Turbulent fluctuation in the edge region in magnetically confined fusion devices plays important roles in core plasma transport[1,2] as well as in transport in the scrape-off layer (SOL).[3] It is considered as a cause of anomalous transport that degrades the core confinement[4] or contributes to plasma wall interaction.[5,6] The origin of the fluctuation is a spatial gradient of plasma temperature or density that drives various types of electrostatic turbulences, such as drift wave and the ion temperature gradient mode. An MHD activity can also drive electromagnetic turbulent fluctuation in the plasma.[7,8] In the analysis of the fluctuation, the spatial distributionand propagation direction/speed of the fluctuation with respect to the magnetic field structure are important to understand the driving mechanism of the fluctuation and the effects on the transport. For this purpose, a gas puff imaging (GPI) system is a viable tool that can provide a spatial (2-D) image of the fluctuation with relatively high spatial and temporal resolutions by localizing the emission from the peripheral region with auxiliary gas injection.[9–12]

Heliotron devices, such as the Large Helical Device (LHD), have special features in the edge magnetic field structure, where the stochastic magnetic field layer is formed due to overlapping of different magnetic mode structures.[13,14] Because of the strong poloidal field and magnetic shear at the edge region of LHD, the divertor leg flux tubes are mostly directed in the poloidal direction and deformed significantly before reaching the divertor plates. It is, therefore, of importance to investigate the edge turbulence characteristics in such a configuration, in order to understand the impact of the magnetic field structure on the turbulence and on the transport for future optimization in a reactor. For this purpose, we are developing a GPI system to measure fluctuation in the edge region of LHD. In LHD the distance from the port at the vacuum vessel to the plasma is long, which decreases the photon flux to the detector. It is also necessary to locate the detector away from the device to reduce neutron flux

from the plasmas. In this article, we present the details of the design of the GPI system to overcome these constraints and its performance obtained in experiments.

II. OPTICAL SYSTEM

The GPI system consists of an optical system that splits the image from the plasma into four different wavelengths, of an image intensifier (II) to amplify the images, and of a fast camera to record the images. In order to avoid direct exposure of the II and the camera to the neutron flux from the plasmas, they are located away from the plasma by transferring the image with image bundle fibers, and are shielded in a box. We first describe the optical system, followed by the II and camera, and the shield box.

The optical system is directly installed at the view port, an ICF152 fused silica window, at the outboard side of the torus. The line of sight (LOS) of the optical system is shown in Fig. 1(a). In the figure, the pink surface represents the "nominal" last closed flux surface (LCFS) of the plasma, since due to the edge stochastization, a strict definition of the LCFS is difficult in LHD. The winding lines around the LCFS represent the magnetic field lines of the divertor legs. The red and yellow colors of the lines indicate the field lines connected to the right and left divertor arrays, respectively. The optical system views the plasma downward, such that the LOS is almost tangential to the divertor leg field lines at the bottom of the torus. The distance from the viewing port to the plasma at the bottom of the torus is about 5 m. As shown in the field of view (FOV) in Fig. 1(b), the LOS passes through the edge plasma just outside the envelope of the LCFS. The measurement area is a circle with a diameter of about 20 cm at the bottom of the torus.

The system is designed to record four images of different wavelengths simultaneously, H_α/D_α (656 nm), HeI (1s2p–1s3d, 587.6, 667.8, and 706.5 nm). The selection of the He I wavelength anticipates obtaining a fluctuation of electron temperature (T_e) and density (n_e) from the line ratios by using collisional radiative (CR) models in the future.

Schematics of the optical system are shown in Fig. 2. The image of the plasma is reflected by a plane mirror of 150 mm diameter, focused by a field lens of focal length 50 mm, F1.4, and collimated by an achromatic lens of focal length 50 mm. The image is first separated by a dichroic mirror (DM587/656) (>90% reflectance at 350.0–594 nm and >93% transmittance at 605–1200 nm). The transmitted image is separated further by a dichroic mirror (DM667/706) (>90% reflectance at 350.0–671 nm and >93% transmittance at 703–1200 nm). The reflected light of DM667/706 is split by a beam splitter (BS) (20% ± 10% reflectance and 80% ± 10% transmittance). Finally, the four images are filtered with custom-made bandpass filters with transmittance of >90%, and full width at half maximum (FWHM) of 3.0 nm at the central wavelengths of 587.5, 706.0, 668.0, and 656.0 nm, respectively.

Each image of a different wavelength is focused onto the image bundle fibers of 2.5 mm diameter (50 000 pixels, NA = 0.22, 5.5 m long, each) by a focus lens. The four bundle image fibers are collected into one bundle at the common end [within a square of 5.7 × 5.7 mm^2 as shown later in Fig. 4(b)], which is 4 m away from the torus. The common end of the fiber is connected to the II (C10880-11C, Hamamatsu Photonics Co., Ltd.) by a coupling lens. The parameters of the above-mentioned lens, the mirrors, the splitter, and the coupling lens of the optical systems are listed in Table I.

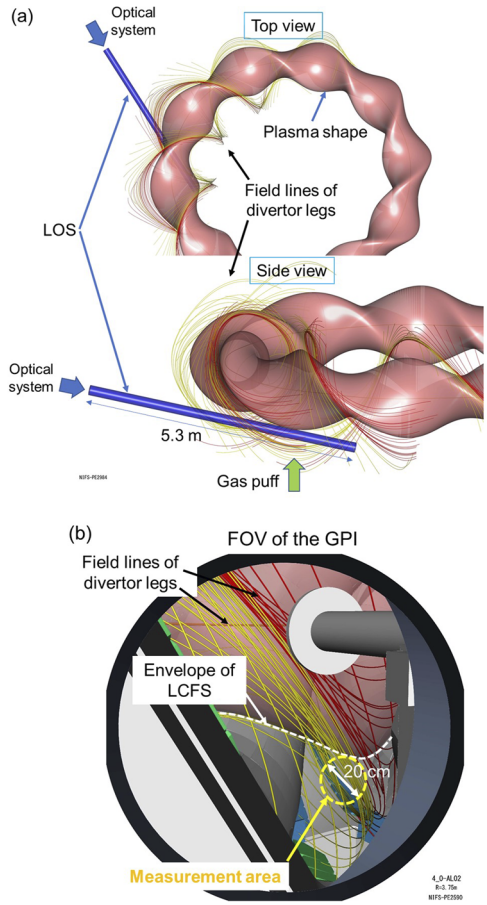

FIG. 1. (a) Line of sight (LOS) of the GPI optical system. (b) Field of view of the optical system. The measurement area is a circle with a diameter of 20 cm just outside the LCFS.

Shown in Table II is the throughput of the image of differing wavelength from the plane mirror 1 to the II, which is calculated based on the values in Table I. Figure 3(a) shows the estimated photon flux to the optical system (the port window) for four wavelengths as a function of T_e. Here we assume n_e of 10^{19} m^{-3} as the nominal plasma density along the divertor leg at the bottom of the torus (5 m away from the port), and 5% of He and hydrogen neutrals. The photon emissivity coefficients, which are a function of T_e and n_e, were taken from the OPEN-ADAS database[15] to calculate the photon flux to the optical system.

The photon flux tends to increase with T_e. H_α/D_α (656 nm) has the highest photon flux, which is more than a factor of 3 higher than He I 587.6 nm at the maximum value around 100 eV. This is the reason why the throughput of 656 nm is designed to be lower than others, which helps to maintain the throughput of He I 667.8 nm as large as possible. It is also noted that the flux of 706.5 nm is low, which constrains the performance of the system to obtain enough signal-to-noise ratio for all wavelengths.

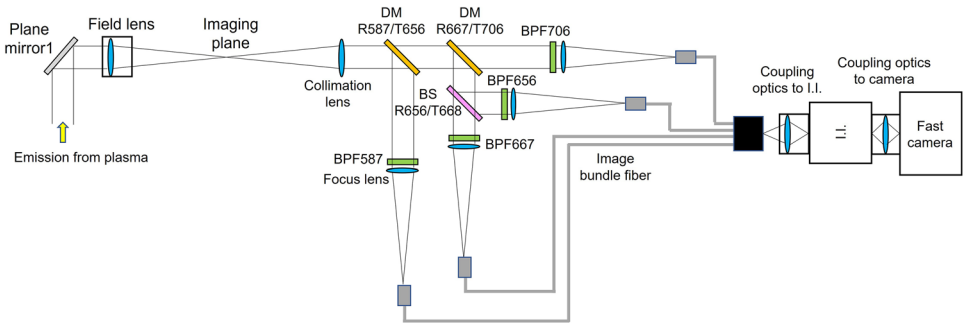

FIG. 2. Schematics of the optical system. DM = dichroic mirror, BS = beam splitter, and BPF = bandpass filter. The plane mirror 2 for 706.5 nm is not shown in the figure.

The images of the four wavelengths are amplified in the II with a photocathode of GaAsP, which has very high sensitivity in the visible range. The quantum efficiency for the four wavelengths is indicated in Table II. Based on the photon flux of Fig. 3(a), the throughput, and the quantum efficiency in Table II, the signal-to-noise ratio (S/N) at the II output can be calculated using the formula

$$\frac{Signal}{Noise} = \frac{I_p}{i_p} \approx \frac{\eta P_{ch}}{\sqrt{F\eta P_{ch} 2B}}, \quad (1)$$

where I_p and i_p are currents of the signal and noise at the anode of the II, respectively. η, P_{ch}, and B are the quantum efficiency of the photocathode, photons per MCP channel of the II (diameter = 13 μm), and frequency bandwidth, respectively. F is a noise figure of the MCP, and we used 1.2 as a typical value. Results are plotted in Figs. 3(b)–3(e) as a function of T_e for a different frequency bandwidth to show the general trend. It is noted that the S/N changes depending on the various discharge conditions, such as a He puff

TABLE I. Parameters of the optical components.

	Reflectance (%)	Transmittance (%)
Plane mirror 1	87	
Field lens (f50 nm, F1.4)		80
Collimation lens (f50 nm)		98
DM R587/T656	90 (@350–594 nm)	93 (@605–1200 nm)
DM R668/T706	90 (@350–671 nm)	93 (@703–1200 nm)
BS R656/T668	20 (@400–700 nm)	80 (@400–700 nm)
Plane mirror 2 (for 706.5 nm)	98	
Focus lens (f50 mm, F2.0)		97
Bandpass filters		90
Image bundle fiber		80
Coupling optics to II		90

TABLE II. Throughput from plane mirror1 to the II and quantum efficiency of the photocathode.

	Throughput (%) (plane mirror1 to II)	Quantum efficiency (%) @photocathode
656 nm	8	30
587.5 nm	39	45
667.8 nm	29	25
706.5 nm	36	15

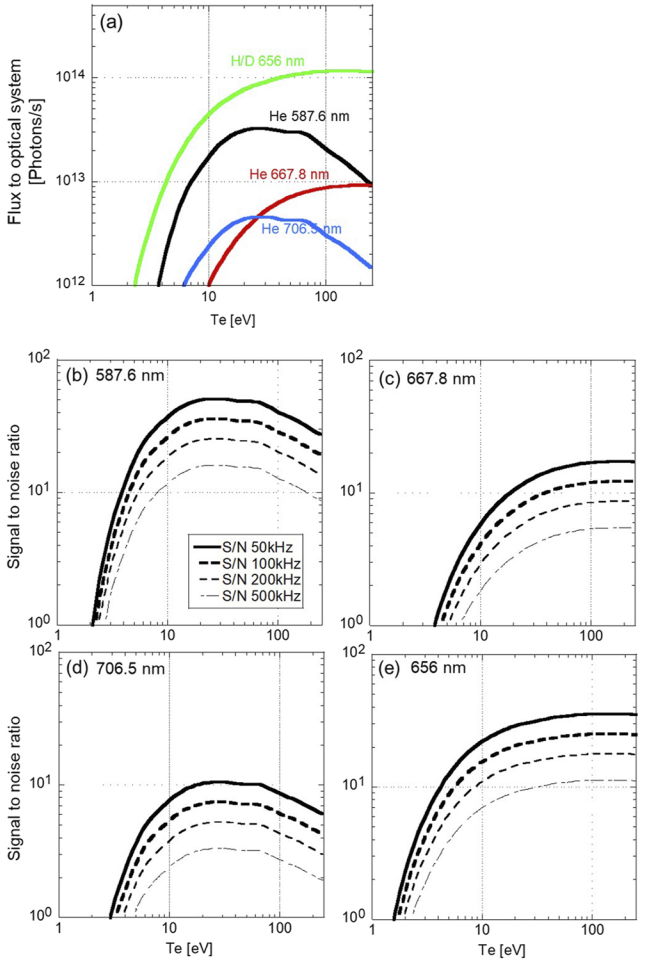

FIG. 3. (a) Photon flux to the optical system (port window) with $n_e = 10^{19}$ m^{-3} as the nominal plasma density along the divertor leg (5 m away from the port), and 5% of He and hydrogen neutrals. (b)–(e) Estimated signal-to-noise ratios for HeI 587.6, 667.8, 706.5 nm, and H_α/D_α 656 nm, respectively.

amount, its penetration into the plasma, and the magnetic field configuration.

In the cases of He I 587.5 nm and H_α/D_α, the S/N are far above ten at >10 eV with 100 kHz. The values are good enough for fluctuation measurements at the edge region, which is expected to be 10%–20% of the mean field typically. In the case of He I 667.8 and 706.5 nm, the S/N is around 10 or slightly less with 100 kHz at ~30 eV for the assumed plasma parameters. This is marginal for measuring the edge fluctuation. The low S/N of 706.5 nm is due both to its low photon emissivity coefficient, and to the low quantum efficiency of the photocathode at the wavelength range. This can be improved with an image bundle fiber with a larger diameter to collect more photons or with a photocathode of GaAsP with extended sensitivity toward a longer wavelength. The former is currently being undertaken. There is also a novel approach to improve the S/N by removing the noise component from a signal as attempted in Ref. 12.

The output image of the II is reduced in size by 0.67 and coupled to a fast camera (Fastcam SA4, Photron Co., Ltd.) with a coupling lens (A11669, 3:2), which further reduces the image size by 2/3, resulting in a diameter of 1.12 mm for each image corresponding to the four wavelengths. The four images are detected with a pixel of 20 μm (an optical fill factor of 0.52). As a result, given that a sufficient number of photons are detected at each pixel, the spatial resolution of the optical system is about 3 mm. As shown in Fig. 3, however, the S/N degrades with increasing sampling frequency. In such a case, a binning of pixels is required to recover the S/N at the cost of the spatial resolution. The active pixels of the camera are 192 × 128 at 100 kHz, which are marginal to cover the four images. The sampling frequency of the camera can be increased up to 500 kHz but with reduced active pixels.

In order to protect the II and the camera from the neutron flux and the magnetic field, they are located about 4 m away from the torus, as described above. They are shielded by a polyethylene block, 10 cm thick, and a lead shield, 15 mm thick inside. Inside the lead shield, an iron shield, 6 mm thick, covers the camera and the II to protect against the magnetic field of about 10 G in a vertical direction at the location. The system has been working without malfunction for more than two experiment cycles.

III. RESULTS

Figure 4(b) shows the images obtained by the system with 50 kHz sampling frequency, where He was puffed by an SSGP (supersonic gas puff),[16,17] which is situated at the bottom of the plasma, as shown in Fig. 1(a). The amount of He puff was 1.93×10^{22} atoms/s with two times 1 ms pulse. The timings of the puffs are shown in Fig. 6(b). Deuterium was puffed by a separated valve, which is situated 72° away from the SSGP in toroidal direction. The deuterium puff rate was of order of 10^{22} molecules/s of 1.5 s pulse with a ramp-up wave form to ramp up the plasma density, as shown in Fig. 6. Clear images were obtained for all wavelengths, and slightly different patterns were recognized for different wavelengths. In this measurement, ND (neutral density) filters of 10% and 5% transmittance were used for He I 587.6 nm and Da 656 nm,

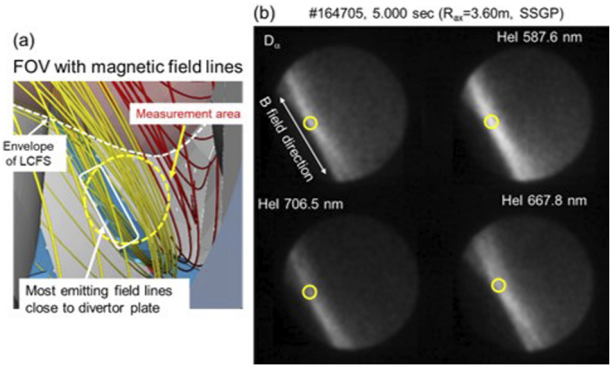

FIG. 4. (a) Enlarged FOV of the optical system. (b) Images obtained by the GPI system for different wavelengths. No. 164705, at 5.000 s with 50 kHz sampling frequency. The bright stripes in the images correspond to the field lines close to the divertor plate indicated in the figure (a). The circles in the figure indicate the location of the data taken for Figs. 6(b) and 6(c).

respectively, in order to adjust the intensity of the different wavelengths into the dynamic range of the camera. As compared to the FOV in Fig. 4(a), the stripe of the image corresponded to the divertor leg field lines close to the divertor plate.

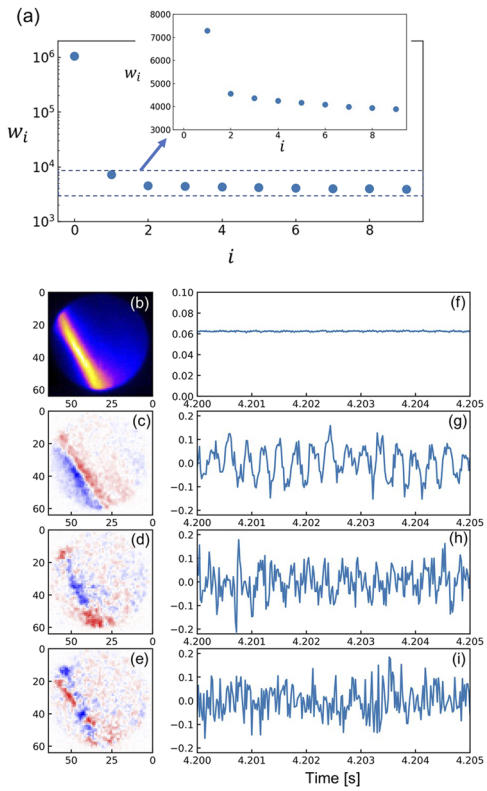

FIG. 5. Analysis of the GPI image with singular value decomposition. (a) Singular values for i = 0–9. (b)–(e) The spatial structure of *U* corresponding to the singular values of i = 0–3. (f)–(i) The time domain components of *V* with i = 0–3, respectively.

In order to analyze the fluctuation, singular value decomposition (SVD) was applied to the data. The images of n x m matrix A with n pixels and m frames were decomposed as

$$A = UWV^t, \quad (2)$$

where U and V^t are the n × r and r × m matrices, respectively.[18] r is the rank of A. The columns of U and V^t are the orthogonal vectors in space and time, respectively. W is a diagonal matrix of r × r, and the non-zero diagonal components, w_i, are the singular values. The square of w_i is a measure of the contribution from a particular component to the total fluctuation power. The results are plotted for He I 587.6 nm in Fig. 5. Figure 5(a) shows the singular values w_i up to i = 9. Figures 5(b)–5(e) are the spatial structure of U corresponding to the singular values of i = 0–3, and Figs. 5(f)–5(i) are the time domain components of V with i = 0–3, respectively. The component of i = 0 represents the most dominant structure, which is almost constant during the time window analyzed. As the direction of the magnetic field lines is indicated in Fig. 4(b), in the i = 1–3 the image is decomposed to a fluctuation perpendicular to the magnetic field lines, as in Fig. 5(c) with i = 1, and parallel to the field lines as in Fig. 5(d) with i = 2, respectively. The spatial pattern of Fig. 5(e) shows a more complex higher mode structure. The approximate size of the spatial structure of each component is estimated as follows: i = 0:3.1 cm in perpendicular to the magnetic field, i = 1:2.2 cm in perpendicular to the magnetic field, i = 2:9.4 cm along the magnetic field, i = 3:<3 cm. In Figs. 5(g) and 5(h), the fluctuations of i = 1 and 2 components have an oscillation around 3 kHz, while their phases are shifted by each other. As seen in the singular values of Fig. 5(a), the fluctuation perpendicular to the field lines dominates over those with i ≥ 2, indicating the existence of strong cross-field transport such as ballistic transport, e.g., blobs.[19,20] We could successfully obtain clear decomposition of the fluctuations to perpendicular and parallel components for all other wavelengths. Clear spatial structure of the fluctuation was also obtained by the SVD analysis with 100 kHz sampling frequency (not shown in this contribution).

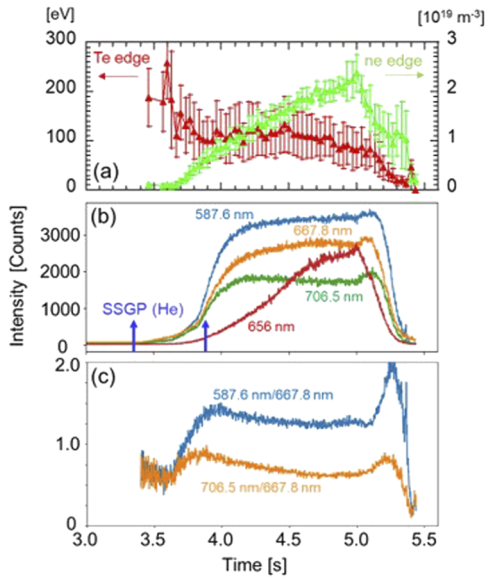

FIG. 6. Time evolutions of (a) edge T_e and n_e in the stochastic layer outside of LCFS measured by a Thomson scattering system, (b) intensity of different wavelengths taken from the location indicated in Fig. 4(b), and (c) ratios of He I intensity. He was puffed at 3.3 and 3.8 s with 1.93×10^{22} atoms each. No. 164705, a density ramp-up discharge.

Figure 6 shows time evolutions of intensity of each wavelength during density ramp-up discharge, where the edge T_e and n_e change substantially during the ramp-up. The edge T_e and n_e were measured by a Thomson scattering system. The location of the data taken for the analysis is indicated in Fig. 4. During the discharge, the ratios of He I intensity, 587.5/668.0 nm and 706.0/668.0 nm, change as shown in Fig. 6(c), as expected from the CR model of He. While derivation of the fluctuation associated with T_e and n_e is underway and left for future work, the results indicate at least the usefulness of the obtained data for such analyses.

These results demonstrate that the present GPI system is viable to measure the spatial distribution of turbulent fluctuations of different wavelengths simultaneously with enough signal-to-noise ratios for fluctuation analyses.

IV. SUMMARY

A GPI system has been developed to measure edge fluctuation in LHD. The optical system splits the image from the plasma into four different wavelengths, H_α/D_α (656 nm), HeI (1s2p–1s3d, 587.6, 667.8, and 706.5 nm). The split images are amplified by the image intensifier and recorded with a fast-framing camera. The obtained images are successfully decomposed to a structure perpendicular and parallel to the magnetic field lines with the SVD method. It is also found that the line ratios of He I intensity alter during the change of edge T_e and n_e, as expected from the CR model. These results demonstrate the feasibility of the GPI system to measure the spatial structure of edge fluctuation with different wavelengths simultaneously. Further improvement of the signal-to-noise ratio with a new image bundle fiber of wider diameter, and the CR model analysis to provide fluctuation associated with T_e and n_e are in progress.

ACKNOWLEDGMENTS

The authors are grateful to the LHD experiment group for the excellent operation of the device. This work was financially supported by JSPS KAKENHI Grant No. 19H01878; NIFS Budget Nos. ULPP026, NIFS19KLPP057, and NIFS22KIPH010; and the Chinese National Natural Science Foundation (Grant No. 11820101004).

AUTHOR DECLARATIONS

Conflict of Interest

The authors have no conflicts to disclose.

Author Contributions

Masahiro Kobayashi: Conceptualization (lead); Data curation (lead); Funding acquisition (equal); Writing – original draft (lead); Writing – review & editing (lead). **Satoshi Ohdachi**: Data curation (supporting); Formal analysis (lead); Funding acquisition (equal). **Yuhong Xu**: Conceptualization (supporting); Funding acquisition

(equal); Project administration (equal). **Wei Li**: Data curation (supporting). **Akihiro Shimizu**: Data curation (supporting); Project administration (lead); Writing – original draft (supporting). **Jun Cheng**: Investigation (supporting).

DATA AVAILABILITY

The data that support the findings of this study are openly available in LHD data repository at https://www-lhd.nifs.ac.jp/pub/Repository_en.html.

REFERENCES

[1]K. Ida *et al.*, Nucl. Fusion **61**, 016012 (2021).
[2]K. Tanaka *et al.*, Nucl. Fusion **59**, 126040 (2019).
[3]Y. Xu *et al.*, Nucl. Fusion **51**, 063020 (2011).
[4]P. C. Liewer, Nucl. Fusion **25**, 543 (1985).
[5]M. Kobayashi *et al.*, Phys. Rev. Lett. **128**, 125001 (2022).
[6]X. Chu *et al.*, Nucl. Fusion **62**, 066021 (2022).
[7]M. Z. Tokar, Phys. Rev. Lett. **91**, 095001 (2003).
[8]B. A. Carreras and P. H. Diamond, Phys. Fluids B **1**, 1011 (1989).
[9]R. J. Maqueda *et al.*, Rev. Sci. Instrum. **74**, 2020 (2003).
[10]M. Agostini *et al.*, Rev. Sci. Instrum. **77**, 10E513 (2006).
[11]S. J. Zweben *et al.*, Rev. Sci. Instrum. **88**, 041101 (2017).
[12]T. Nishizawa *et al.*, Rev. Sci. Instrum. **92**, 103501 (2021).
[13]N. Ohyabu *et al.*, Nucl. Fusion **34**, 387 (1994).
[14]M. Kobayashi *et al.*, Fusion Sci. Technol. **58**, 220 (2010).
[15]See https://open.adas.ac.uk/ for information about photon emissivity coefficients.
[16]A. Murakami *et al.*, Plasma Fusion Res. **5**, S1032 (2010).
[17]A. Murakami *et al.*, Plasma Phys. Controlled Fusion **54**, 055006 (2012).
[18]S. Ohdachi *et al.*, Plasma Sci. Technol. **8**, 45 (2006).
[19]S. I. Krasheninnikov *et al.*, Phys. Plasmas **16**, 014501 (2009).
[20]H. Tanaka *et al.*, Phys. Plasmas **17**, 102509 (2010).